https://doi.org/10.1038/s44306-024-00020-9

# Multiferroic kinks and spin-flop transition in $Ni_2InSbO_6$ from first principles

Check for updates

Ryota Ono[1,2] ✉, Igor Solovyev[2] & Sergey Artyukhin[1]

Magnetoelectric multiferroics are key materials for next-generation spintronic devices due to their entangled magnetic and ferroelectric properties. Spiral multiferroics possess ferroelectric polarization and are particularly promising for electric control of magnetism and magnetic control of ferroelectricity. In this work, we uncover long-period incommensurate states characterized by unique multiferroic kinks in corundum nickelate $Ni_2InSbO_6$, a member of a promising family of polar magnets. Utilizing a 2-orbital $S = 1$ model, we derive formulas for Heisenberg and anisotropic magnetic exchanges and magnetically-induced polarization, enabling their calculations from first principles. We use these parameters in Monte Carlo and Landau theory-based calculations to reproduce experimentally observed magnetic structures and polarization dependence on the magnetic field. We predict magnetic phase transitions between flat spiral, conical spiral, canted antiferromagnetic and ferromagnetic states under increasing magnetic fields. Kinks in the spiral phases repel each other through a Yukawa-like potential arising from exchange of massive magnons. We also find that suitably directed electric fields can be used to stabilize the ferromagnetic and spiral states. The findings open a new pathway to predictive first-principles modelling of multiferroics and will inspire experiments and technological applications based on multiferroic kinks.

In magnetoelectric multiferroics, a magnetic order coexists and interacts with a ferroelectric one. Several microscopic scenarios of why such coexistence may occur and how the magnetic order can affect the electric polarization have been established[1–5] and the work is rapidly progressing in this direction. Understanding such interactions between the magnetic and electric degrees of freedom is of great importance from both the fundamental and practical points of view. A special attention is paid to the mutual control of the magnetic structure and the electric polarization by applying the magnetic or electric field. For instance, the external magnetic field can control the magnetic structure, while also changing the ferroelectric polarization. Conversely, the external electric field can be used to control the magnetic structure[6].

There are two main types of multiferroic (MF) materials[4]. In type-I multiferroics the crystal structure itself is ferroelectric, irrespectively of the magnetism. However, the electric polarization can still be controlled by changing the magnetic structure. In type-II MF the crystal structure is centrosymmetric, but the inversion symmetry can still be broken by a magnetic order, which leads to the ferroelectric polarization. An interesting aspect of the type-I materials is that many of them develop chiral magnetic structure, driven by antisymmetric Dzyaloshinskii-Moriya (DM) interactions in the non-centrosymmetric crystal structure. This chirality can be controlled by the magnetic field, presenting another interesting avenue for magnetoelectric control in type-I materials. For instance, a very special type of the chiral magnetic structure is the skyrmion lattice, which has been intensively studied in the context of MF applications in $Cu_2OSeO_3$ and $GaV_4S_8$[7,8].

$Ni_2InSbO_6$ (NISO) is one of such chiral MFs. Its low temperature structure has a polar (non-centrosymmetric) rhombohedral $R3$ space group[9,10] similar to well known MF corundum derivative $Ni_3TeO_6$[11,12]. A number of polar corundum derivatives have recently been synthesized and materials with above room temperature magnetism have been found[13,14]. These are promising candidates for magnetoelectric applications, in some of which polarization switching has been predicted [15]. Previous studies[16] revealed an incommensurate antiferromagnetic proper-screw spiral (helix) within each Ni layer, with a long periodicity of 30 unit cells. The polarization along the threefold rotation axis changes quadratically with the magnetic field due to variations in the spiral order induced by the field[16]. In addition, recent experiments have revealed a spin-flop (SF) transition upon applying the magnetic field along the threefold rotation axis[17,18]. However, the detailed microscopic analysis of these observations is lacking. The

[1]Quantum Materials Theory, Italian Institute of Technology, Via Morego 30, 16163 Genova, Italy. [2]Research Center for Materials Nanoarchitectonics (MANA), National Institute for Materials Science (NIMS), 1-1 Namiki, Tsukuba, Ibaraki 305-0044, Japan. ✉e-mail: ryota.ono.gm@gmail.com

phenomenological mechanisms of the magneto-electric coupling considered so far[19–21] are not universal and are influenced by system-dependent factors. Therefore, it is important to construct realistic models of these materials with interacting spins and magnetically-induced polarization, starting from the modern theory of polarization in terms of Berry phases and Wannier centers[22–24] and using model parameters obtained from first-principles calculations. According to such calculations in the generalized gradient approximation (GGA), NISO can be regarded as an $S = 1$ material. In the corundum structure, each $Ni^{2+}$ ion is located in a distorted octahedron of $O^{2-}$ ions. Therefore, the Ni 3*d* states split into triply degenerate $t_{2g}$ and double degenerate $e_g$ manifolds. The $t_{2g}$ states are fully occupied and do not significantly contribute to magnetism. On the other hand, the $e_g$ states are half-filled and form a group of narrow bands near the Fermi level, which are mainly responsible for the $S = 1$ physics. Thus, we can greatly simplify our analysis by constructing the 2-orbital model for these bands and extracting all parameters of the model from the first principles calculations in the Wannier basis.

Here we model the exchange interactions *and* magnetically-induced polarization emerging from such realistic 2-orbital $e_g$ model at the half-filling. After extracting the parameters of electronic Hubbard-like model from the first principles calculations, we employ the superexchange theory, which in our case is formulated as a first-order perturbation theory for the Wannier functions with respect to the hopping parameters. For the exchange interactions, the treatment is equivalent to the standard second-order perturbation theory for the magnetic energy, which in the Wannier basis results in the expression for the spin dependent electric polarization. Our models highlight the emergence of intriguing cross-coupling phenomena in NISO. Specifically, we explore the SF transitions and a crossover to the multiferroic kink array state, both induced by the external magnetic field along the threefold axis. The kinks contribute ferroelectric polarization opposite to that of the collinear state and their energetics can be rationalized in terms of repulsion through the Yukawa-like potential and the competition between the DM and magnetic field setting their chemical potential. Additionally, using a continuous theory, we explore the possibility of cross-control of magnetic (electric) order by an electric (magnetic) field.

## Results

### Basic electronic structure, electronic and spin model for NISO

Results of electronic structure calculations using the experimental crystal structure, shown in Fig. 1a[10], in GGA[25,26] with the spin-orbit coupling (SOC) for a nonmagnetic state are illustrated in Fig. 1e. These calculations clearly reveal two groups of the Ni 3*d* bands: six $t_{2g}$ bands (per two Ni sites) around − 1 eV and four $e_g$ bands around the Fermi level. In NISO, the $t_{2g}$ bands are fully occupied and nonmagnetic, while the magnetic properties are mainly associated with the $e_g$ bands. Therefore, we pick this group of states to construct a realistic Hubbard-type model, which would capture the magnetic behavior of NISO. Such Hubbard model has the form:

$$\hat{\mathcal{H}} = \sum_{ij}\sum_{ab}\sum_{\sigma\sigma'} t_{ij}^{ab\sigma\sigma'}\hat{c}_{ia\sigma}^{\dagger}\hat{c}_{jb\sigma'} + H_{\text{on-site}}, \tag{1}$$

where $a$ and $b$ ( = 1 or 2) label the $e_g$ orbitals, and $H_{\text{on-site}}$ stands for the on-site Coulomb interactions, which are specified by the intra-orbital interaction $U$, Hund's coupling $J_H$ and inter-orbital interaction $U' = U - 2J_H$[27]. $\hat{c}_{ia\sigma}^{\dagger}$ ($\hat{c}_{ia\sigma}$) in Eq. (1) stands for the creation (annihilation) of an electron on the Wannier orbital $a$ of the Ni site $i$ with the spin $\sigma$. The parameters of the one-electron part, $t_{ij}^{ab\sigma\sigma'}$, are defined as the matrix elements of GGA Hamiltonian in the Wannier basis. Since the basis is complete for the $e_g$ bands, these parameters perfectly reproduce the original band structure in GGA (see Fig. 1e). The main sources of the SOC in NISO are the 5*p* states of the heavy In/Sb atoms. Therefore, it is important to include the SOC *before* the wannierization, at the level of regular GGA calculations. Then, although the Wannier functions are formally associated with the Ni $e_g$ states, the SOC of the heavy In/Sb atoms will still contribute to the matrix elements $t_{ij}^{ab\sigma\sigma'}$, which can be diagonal as well as off-diagonal with respect to the spin indices.

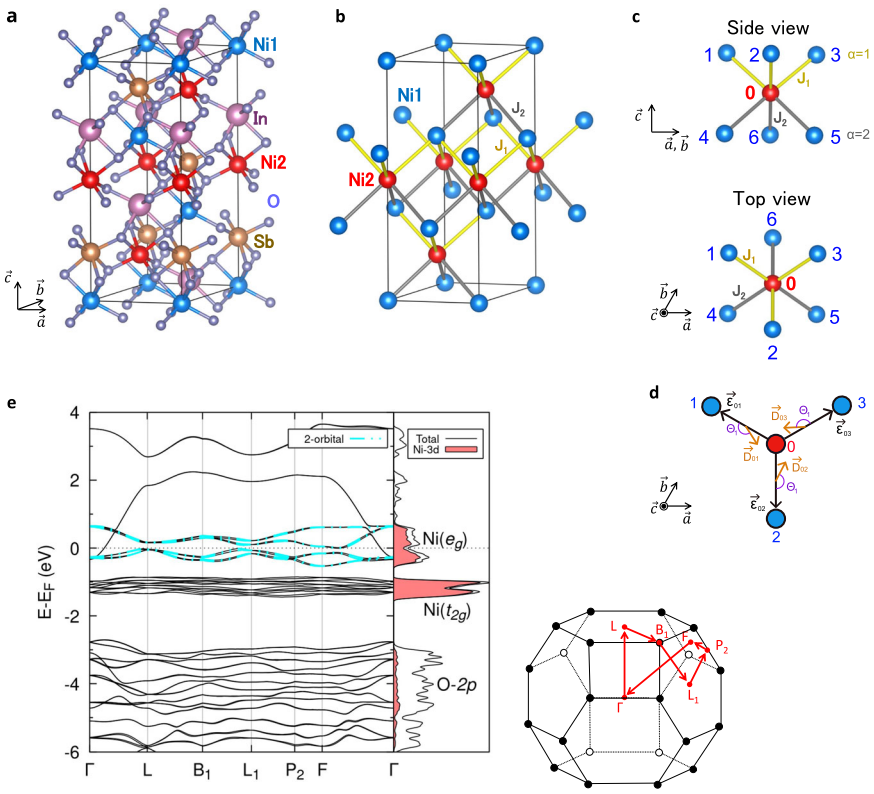


**Fig. 1 | Crystal structure and electronic structure of NISO. a** Hexagonal cell of NISO. **b** Ni ions in the hexagonal cell. Only the closest neighbors coupled with exchange constants $J_1$ and $J_2$ are shown with yellow and gray lines, respectively. **c** $J_1$ and $J_2$ bonds from side view and top view around a Ni ion. **d** Definition of DM vector parameters. This figure explicitly depicts parameters for $\alpha = 1$ bond type. **e** Electronic structure of a rhombohedral unit cell of NISO around Fermi level calculated within GGA (solid black line) and 2-orbital model constructed by MLWF method (cyan dashed line). The inset shows a schematic of the k-path in the Brillouin zone for the rhombohedral unit cell.

Next, we map this low energy electronic model onto the spin model employing for these purposes the superexchange theory. In the atomic limit, the ground state corresponding to the high-spin $S = 1$ state at half-filling is described by the single Slater determinant. The same holds for the one-electron and one-hole $e_g$ states emerging in the superexchange theory in the process of virtual excitations. Therefore, here we essentially deal with the one-electron theory. This results in the spin Hamiltoninan:

$$\mathcal{H}_s = \sum_{<ij>}\left(-J_{ij}\vec{e}_i\cdot\vec{e}_j + \vec{D}_{ij}\cdot(\vec{e}_i\times\vec{e}_j) + \vec{e}_i\cdot\vec{\Gamma}_{ij}\vec{e}_j\right), \tag{2}$$

where $\vec{e}_i$ stands for the classical spin vector at site $i$, the first term is the isotropic interaction, the second term is the anisotropic Dzyaloshinskii-Moriya interaction and the last term is the (traceless) symmetric exchange anisotropy[28].

Similarly, the expression for the magnetically-induced polarization is given by

$$\vec{P}_s = \sum_{<ij>}\left(\vec{\mathrm{P}}_{ij}\vec{e}_i\cdot\vec{e}_j + \vec{\vec{\boldsymbol{\mathcal{P}}}}_{ij}\cdot(\vec{e}_i\times\vec{e}_j) + \vec{e}_i\cdot\vec{\vec{\mathbf{\Pi}}}_{ij}\vec{e}_j\right), \tag{3}$$

where the first term describes isotropic exchange striction, while the following terms originate form the antisymmetric and the (traceless) symmetric anisotropy[29–31]. This model is derived in the framework of the modern theory of polarization in solids[22–24], using perturbation expansion of the Wannier functions.

Since the $R3$ group has only one three-fold rotation axis (along $z$ in the chosen coordinates), all bonds with the same distance should be transformed into each other by the $\hat{C}_3^z$ rotation. To illustrate this, consider the bonds surrounding a Ni ion labeled as 0 in Fig. 1c. We index its Ni neighbors in the layer above as $j = 1, 2, 3$, which are classified as bond type $\alpha = 1$. Conversely, the Ni ions in the layer below, indexed as $j = 4, 5, 6$ and categorized as bond type $\alpha = 2$, are at a slightly longer distance. The vectors connecting ion 0 with ions $j = 1, 2, 3$ are expressed as $\vec{\epsilon}_{0j} = (\epsilon_{0j}^{\parallel}\cos(2\pi j/3), \epsilon_{0j}^{\parallel}\sin(2\pi j/3), \epsilon_{0j}^{\perp})$, where $\epsilon_{0j}^{\parallel}$ and $\epsilon_{0j}^{\perp}$ are the lengths of the vector components parallel and perpendicular to the Ni layer, respectively (see Fig. 1d). For $j = 4, 5, 6$, similar formula applies, with the same $\epsilon_{0j}^{\parallel}$, but a slightly different $\epsilon_{0j}^{\perp}$ and with the arguments of sin and cos incremented by $\pi$. Then, the DM vectors are as follows:

$$\vec{D}_{0j}^{\alpha} = \left(d_{\alpha}^{\parallel}\cos\theta'_{j,\alpha}, d_{\alpha}^{\parallel}\sin\theta'_{j,\alpha}, d_{\alpha}^{\perp}\right), \tag{4}$$

where $\theta'_{j,\alpha} = 2\pi j/3 + \theta_{\alpha}$, $d_{\alpha}^{\perp}$ and $d_{\alpha}^{\parallel}$ are bond-dependent parameters. The DM vectors are antisymmetric: $\vec{D}_{j0}^{\alpha} = -\vec{D}_{0j}^{\alpha}$. Similarly, contributions from the isotropic (Heisenberg) exchange to the magnetically-induced polarization (first term of Eq. (3)) are as follows:

$$\vec{\mathrm{P}}_{0j}^{\alpha} = \left(p_{\alpha}^{\parallel}\cos\theta'_{j,\alpha}, p_{\alpha}^{\parallel}\sin\theta'_{j,\alpha}, p_{\alpha}^{\perp}\right), \tag{5}$$

with symmetric $\vec{\mathrm{P}}_{j0}^{\alpha}$: $\vec{\mathrm{P}}_{j0}^{\alpha} = \vec{\mathrm{P}}_{0j}^{\alpha}$.

An additional single-ion term is allowed in systems $S > 1/2$. However, in the subsequent discussion, we neglect this term, expecting its effect to be minor since the orbital angular momentum matrix elements vanish between $e_g$ orbitals, making SOC inactive. Indeed, in our 2-orbital model, the energy splitting due to SOC inside $S = 1$ triplet results in very tiny $\Delta E \approx 7\ \mu$eV (see Supplementary Note 2). Turning to the magnetically-induced polarization, we calculate the single-ion term by the formula given in ref. 32. However, we also neglect this term as it is spin-independent in this 2-orbital model.

We derive analytical formulas for the symmetric and antisymmetric exchange constants in (2) and magnetically-induced electronic component of the polarization in (3) from the 2-orbital model following the strategy used in refs. 30,31 (see "Methods" for the derivation). For exchange interactions we have:

$$\begin{aligned}
J_{ij} &= \tfrac{1}{3\Delta E}\sum_{\alpha\beta}^{1,2}\left\{-3\left(t_{ij}^{0\alpha\beta}\right)^2 + \mathrm{Tr}(\mathbf{t}_{ij}^{\alpha\beta}\otimes\mathbf{t}_{ij}^{\alpha\beta})\right\},\\
\vec{D}_{ij} &= \tfrac{2}{\Delta E}\sum_{\alpha,\beta}^{1,2} t_{ij}^{0\alpha\beta}\mathbf{t}_{ij}^{\alpha\beta},\\
\vec{\vec{\Gamma}}_{ij} &= \tfrac{2}{\Delta E}\sum_{\alpha,\beta}^{1,2}\left[\mathbf{t}_{ij}^{\alpha\beta}\otimes\mathbf{t}_{ij}^{\alpha\beta} - \tfrac{1}{3}\mathrm{Tr}(\mathbf{t}_{ij}^{\alpha\beta}\otimes\mathbf{t}_{ij}^{\alpha\beta})\vec{\vec{\mathbb{I}}}\right],
\end{aligned} \tag{6}$$

while the parameters for magnetically-induced electronic component of the polarization have the form:

$$\begin{aligned}
\vec{\mathrm{P}}_{ij} &= -\tfrac{2e}{3V\Delta E}\sum_{\alpha,\beta}^{1,2}\left(3\vec{r}_{ij}^{0\alpha\beta}t_{ij}^{0\alpha\beta} - \mathrm{Tr}\left(\vec{\mathbf{r}}_{ij}^{\alpha\beta}\otimes\mathbf{t}_{ij}^{\alpha\beta}\right)\right),\\
\vec{\mathcal{P}}_{ij} &= -\tfrac{2e}{V\Delta E}\sum_{\alpha,\beta}^{1,2}\left(t_{ij}^{0\alpha\beta}\vec{\mathbf{r}}_{ij}^{\alpha\beta} + \vec{r}_{ij}^{0\alpha\beta}\mathbf{t}_{ij}^{\alpha\beta}\right),\\
\vec{\vec{\mathbf{\Pi}}}_{ij} &= -\tfrac{2e}{V\Delta E}\sum_{\alpha,\beta}^{1,2}\left(\vec{\mathbf{r}}_{ij}^{\alpha\beta}\otimes\mathbf{t}_{ij}^{\alpha\beta} + \mathbf{t}_{ij}^{\alpha\beta}\otimes\vec{\mathbf{r}}_{ij}^{\alpha\beta} - \tfrac{2}{3}\mathrm{Tr}\left(\vec{\mathbf{r}}_{ij}^{\alpha\beta}\otimes\mathbf{t}_{ij}^{\alpha\beta}\right)\vec{\vec{\mathbb{I}}}\right),
\end{aligned} \tag{7}$$

where $\Delta E = U + J_H$, $\mathbf{t}_{ij}^{\alpha\beta}$ and $\vec{\mathbf{r}}_{ij}^{\alpha\beta}$ are the spin dependent matrix elements of the hopping and position operator, correspondingly, expanded in Pauli matrices as $\hat{t}_{ij} = t_{ij}^0\otimes\hat{\sigma}_0 + \sum_{\gamma}^{x,y,z} it_{ij}^{\gamma}\otimes\hat{\sigma}_{\gamma}$, $\hat{\vec{r}}_{ij} = \hat{\vec{R}}_{ij}^{0}\otimes\sigma_0 + \sum_{\gamma'} i\vec{R}_{ij}^{\gamma'}\otimes\hat{\sigma}_{\gamma'}$, $\vec{\vec{\mathbb{I}}}$ is a $3\times3$ identity matrix. $J_{ij}$ and $\vec{\mathrm{P}}_{ij}$ are the symmetric isotropic (Heisenberg) exchange (scalar) and exchange striction (vector), while the consecutive terms describe antisymmetric (Dzyaloshinskii-Moriya) exchange and symmetric anisotropic (Ising-like) interactions, respectively. The exchange parameters obtained with this method are summarized in Tables 1 and 2. We find that the significant exchange interactions in NISO predominantly originate from the bonds between Ni2 and its Ni neighbors in the layer above (ions 1,2,3, exchange constant $J_1$) and below (ions 4,5,6, exchange constant $J_2$), as shown in Fig. 1c. The obtained parameters obey $J_2 < J_1$, which can be understood considering geometric Ni-O-Ni angles, ∠(Ni-O-Ni, $J_1$) = 129.38° and ∠(Ni-O-Ni, $J_2$) = 136.75°. Typically, the half-filled 2-orbital model predominantly yields AFM interactions, with FM contributions manifesting as effective suppressions in the AFM iteraction constants. According to the Goodenough-Kanamori rule[33], the bond angle ∠(Ni-O-Ni, $J_1$) being close to 90° compared to ∠(Ni-O-Ni, $J_2$), leads to $J_1$ receiving compensations by the ferromagnetic contributions. Consequently, this results in a smaller magnitude of $J_1$ compared to $J_2$.

We note that the 2-orbital model parameters also provide insight into importance of different terms in Eq. (2) and Eq. (3). As for the magnetic

**Table 1 | Values of isotropic exchanges and DM parameters in NISO [meV]**

| Bond $\alpha$ | Dist. | $J_{\alpha}$ | $d_{\alpha}^{\parallel}$ | $d_{\alpha}^{\perp}$ | $\theta_{\alpha}$ [Deg.] |
|---|---|---|---|---|---|
| 1 | 3.821 | −6.872 | 1.255 | 1.046 | 138 |
| 2 | 3.912 | −13.095 | 1.833 | −1.053 | 64 |

**Table 2 | Values of isotropic term for polarization and corresponding parameters in NISO [$\mu C/m^2$]**

| Bond $\alpha$ | Dist. | $p_{\alpha}^{\parallel}$ | $p_{\alpha}^{\perp}$ | $\theta_{\alpha}$ [Deg.] |
|---|---|---|---|---|
| 1 | 3.821 | 449 | −138 | 75 |
| 2 | 3.912 | 613 | 242 | 180 |

energy, isotropic and antisymmetric exchange contributions are found to be non-negligible (see Supplementary Note 1 for the values of the symmetric anisotropy tensor components). Actually, the relative magnitudes of isotropic and DM interactions indicate that the symmetric anisotropic exchange is inherently small. This fact aligns with Moriya's paper[28] and our analytical formulas (6). These state that the DM interaction is first-order in SOC, whereas the symmetric anisotropy is second-order in SOC. Among the contributions to the polarization, only the isotropic term is found non-negligible. Therefore, in the following we focus mainly on these terms. The actual values of the anisotropic terms of the magnetically-induced polarization and their small effects are detailed in Supplementary Note 3. Consequently, in the following we primarily focus on the isotropic exchange, the DM exchange and the isotropic term of the magnetically-induced polarization.

We note that the antiferromagnetic contribution overestimates the exchange parameters as the 2-orbital model does not take into account ferromagnetic contributions from $t_{2g}$ orbitals and Hund's couplings on non-magnetic ions accurately. Additionally, the relatively small value of the denominator in superexchange theory, specifically $\Delta E = 2.9$ eV, further contributes to potential overestimations in the overall exchange parameters. Using these parameters in the Monte-Carlo simulations in a $30 \times 30 \times 1$ simulation box with periodic boundary conditions, we obtain the transition temperature, overestimating the experimental one by approximately a factor of two. The transition temperature was identified by the peak in the heat capacity in Monte-Carlo simulations using the calculated parameters (Supplementary Note 5). Nevertheless, we emphasize that the main physics discussed in the following is purely originating from the relative strength between isotropic and anisotropic exchanges.

### Magnetic structures in NISO

We now discuss the magnetic ground state obtained from the single-$q$ spiral Ansatz analysis in NISO. The 2-orbial parameters show that the $J_1$ and $J_2$ are very strong and AFM. Thus, we can expect spins in the neighboring layers to be opposite. Since there are four Ni layers in the hexagonal cell, Fig. 1a, the period of the AFM order coincides with the length of the hexagonal c-axis, thus, we have $\vec{q}_C = (0, 0, 0)$. DM interactions modify $q$-vector from a commensurate phase to an incommensurate one by $\delta\vec{q}$. The 2-orbital model parameters show that those bonds fulfill a relation $d_\alpha^{\parallel} > d_\alpha^{\perp}$. This stabilizes spin-spiral states with the propagation vector within the layer. Namely, the $q$-vector is modified as $\vec{q}_{IC} = \vec{q}_C + \delta\vec{q} = (\delta q_x, \delta q_y, 0)$. Then, we can consider the situation given in Fig. 2a, where the spin spiral propagates within a Ni layer.

Magnetic energy contributions from isotropic ($E_{iso}$) and DM ($E_{DM}$) interactions are

$$\begin{aligned} E_s &= E_{iso} + E_{DM} \\ &= \tfrac{1}{4}\Big\{(J_1 + J_2)\Big(12 - \delta q_x^2 - \delta q_y^2\Big) \\ &\quad - 2\sqrt{3}\delta q_x\big(d_1^{\parallel}\sin(\theta_1 - \phi) + d_2^{\parallel}\sin(\theta_2 - \phi)\big) \\ &\quad - 2\sqrt{3}\delta q_y\big(d_1^{\parallel}\cos(\theta_1 - \phi) + d_2^{\parallel}\cos(\theta_2 - \phi)\big)\Big\}. \end{aligned} \tag{8}$$

Then, we take derivative of the energy with respect to $\delta q_x$ and $\delta q_y$, and find the energy minimum at $\delta\vec{q}$,

$$\begin{cases} \delta q_x = \sqrt{3}\big(-d_1^{\parallel}\sin(\theta_1 - \phi) - d_2^{\parallel}\sin(\theta_2 - \phi)\big)/(J_1 + J_2) \\ \delta q_y = \sqrt{3}\big(-d_1^{\parallel}\cos(\theta_1 - \phi) - d_2^{\parallel}\cos(\theta_2 - \phi)\big)/(J_1 + J_2). \end{cases} \tag{9}$$

The wavevector components are plotted in Fig. 2a using the parameters from the 2-orbital model. We see that, approximately, $(\cos\phi, \sin\phi, 0) \perp \hat{n}^{\perp}$, thus, a cycloidal spiral state (Fig. 2b), while the experiment reported a proper-screw spiral state. However, the wave vector and the spiral period, $\delta q_{Ans} \approx 0.034$ (29 unit cells) are in a good agreement with reported experimental values $\delta q \approx 0.029$ (30 unit cells)[9]. Additionally, the symmetric anisotropic interactions tilt the spin-spiral plane. The calculated parameter actually give a small rotation $\approx \pi/8$ (see Supplementary Note 1). Another parameter set, calculated from Green's function method[34], gives a proper-screw type spiral with a very long wave length of 142 unit cells ($\delta q_{GF} \approx 0.007$; see Supplementary Note 4). Since the spin spiral type is not important for the following discussion of magnetic kink generation and magnetically-induced polarization, we use a cycloidal spiral as the ground state of NISO. We note that in this mean-field analysis, the energy does not depend on the rotation of the spiral plane $\phi$. This can be straightforwardly confirmed by substituting the analytical formula for the spiral wave vector Eq. (9) into the energy Eq. (8). The resulting formula yields $E_s = 3((d_1^{\parallel})^2 + (d_2^{\parallel})^2 + 2d_1^{\parallel}d_2^{\parallel}\cos(\theta_1 - \theta_2) + 4(J_1 + J_2)^2)/(4(J_1 + J_2))$, thus, independent of $\phi$.

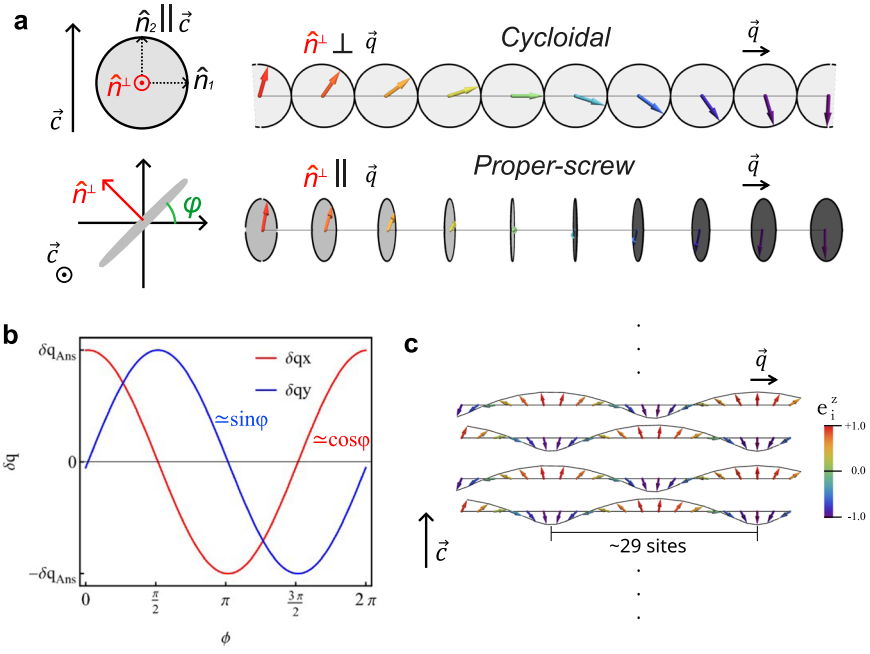


**Fig. 2 | Magnetic ground state as obtained from the single-q spiral Ansatz. a** Definition of the spin-spiral parameters. **b** The components of $\delta q$ minimizing the energy as a function of the spin rotation plane orientation (given by a polar angle $\phi$, where the rotation plane normal is $\hat{n}^{\perp} = (-\sin\phi, \cos\phi, 0)$). The energy is minimized by $\delta q \sim (\cos\phi, \sin\phi, 0)$ which is perpendicular to $\hat{n}^{\perp}$, giving rise to a cycloidal spiral. The horizontal axis indicates the rotation of the spin-spiral plane. **c** The cycloidal spiral ground state for the Hamiltonian, with magnetic exchange constants derived from our superexchange theory. Black lines connecting the sites and spins of neighbors are drawn as a guide.

In order to understand the magnetic ground state and the response to the external magnetic fields in NISO, we also perform classical Monte-Carlo simulations (MCS) of the spin model Eq. (2) with the 2-orbital parameters. Incorporating the Zeeman term $-\sum_i H_z e_i^z$, simulations are carried out on a $30 \times 30 \times 1$ supercell with periodic boundary conditions.

Our MCS reveal the emergence of an anticipated spiral ground state, see Fig. 3a. This result validates the applicability of our single-$q$ spiral Ansatz. Upon the application of an external magnetic field perpendicular to the layer, a SF transition is found. This supports the observations reported in refs. 16–18. Remarkably, before the SF transition, we observe the solitons, favored by DM interaction, shrinking, while the regions between them, with spins along the magnetic field, experiencing a notable increase (Fig. 3b). In comparison to the experimentally determined transition field of approximately 20 T, our calculations yield an overestimated field of approximately 100 T. This discrepancy is attributed to the overestimated exchange parameters and finite size effects in the MCS. Despite the success of the MCS, finite size effects significantly influence important spiral deformations by forcing the spiral to be commensurate with the simulation box. Therefore, in the following we derive and employ a continuous Ginzburg-Landau-type theory.

### 1D continuous model

Application of the external magnetic field can modify the spiral period. Such a phenomenon, often elusive in MCS due to finite size limitations, can result in overlooking of interesting physics like spiral period changes. For instance, De Gennes investigated modifications of the solitonic lattice period by an external magnetic field in liquid crystals[35] and concluded that the spiral period follows the analytical expression:

$$\frac{L(H_z)}{L(0)} = \left(\frac{2}{\pi}\right)^2 K(k)E(k), \tag{10}$$

where $L(0)$ is the original period of the perfect spiral at zero field, and $K(k)$, $E(k)$ are elliptic integrals of the first and second kind, respectively. Here, we formulate a continuous theory to capture such period changes and resulting magnetically-induced polarization without any restriction of the periodicity. As we see from MCS, the obtained magnetic structures are quasi-1D, therefore we can effectively model NISO as a 1D-chain. This is due to the following reasons. First, the spiral lies in the $xy$-plane. Second, important exchanges are only $J_1$ and $J_2$ bonds. They involve the group of bonds connected by the $\hat{C}_3^z$ operation. Those give rise to the energy expression identical to that of a 1D chain.

Figure 4 shows the spin-spiral ground state and the states it deforms into under an external magnetic field perpendicular to the layer, as obtained by minimizing 1D AFM continuous chain energy in Eq. (37). First, application of an external magnetic field generates a kink array state (Fig. 4c, g, k): instead of rotating in space with the constant wave vector, antiferromagnetic order parameter now rotates in a non-uniform fashion. Indeed, when $\vec{A}$ is pointing perpendicular to the magnetic field $\vec{H}$, sublattices cant along the field, which leads to a gain of Zeeman energy, linear in the canting angle (at the expense of the quadratic loss in the antiferromagnetic exchange energy between the sublattices). Thus, the regions with $\vec{A} \perp \vec{H}$ expand, forming plateaus in $A_x$ (Fig. 4c), which increases the gain of the Zeeman energy on canting. In contrast, between the plateaus, kinks in $A_x$ (or solitons) occur where $\vec{A}$ quickly rotates through the field direction. At these points, one sublattice aligns with the field and another – opposite to it, and therefore the gain of Zeeman energy on the canting is not possible. The shape of these kinks is analogous to the solitons in nonlinear dynamics because they are solutions of the Sine-Gordon equation. The continuous model reveals that with further increase of the field strength, the kinks are pushed apart. At a higher field, the flat spiral turns into a conical one and its plane flops perpendicular to the field (Fig. 4b, f, j), which enables a higher gain of Zeeman energy from spin canting along the field. The kinks, present both in the flat and conical spiral phases, can be viewed as particles interacting with each other via exchange of magnons. Further increase of the magnetic field strength drives the transition into SF phase. These transitions are very similar to the one found in our MC simulations (Fig. 3b). However, in this continuous theory, the transition is much smoother due to unrestricted simulation box size.

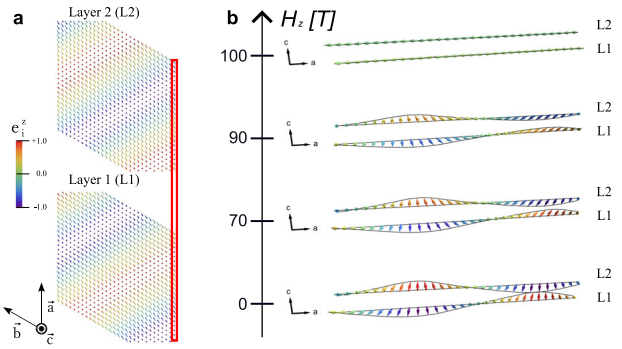


**Fig. 3 | Magnetic structures as obtained from the Monte-Carlo simulations.** **a** Magnetic ground state of NISO as obtained from classical Monte-Carlo simulations. The red rectangle indicates the area, for which we show the spin texture in Panel (**b**). **b** Magnetic structure inside the area, indicated by the red box in Panel (**a**) for different values of an external magnetic field, perpendicular to the spiral plane (three-fold rotation axis).

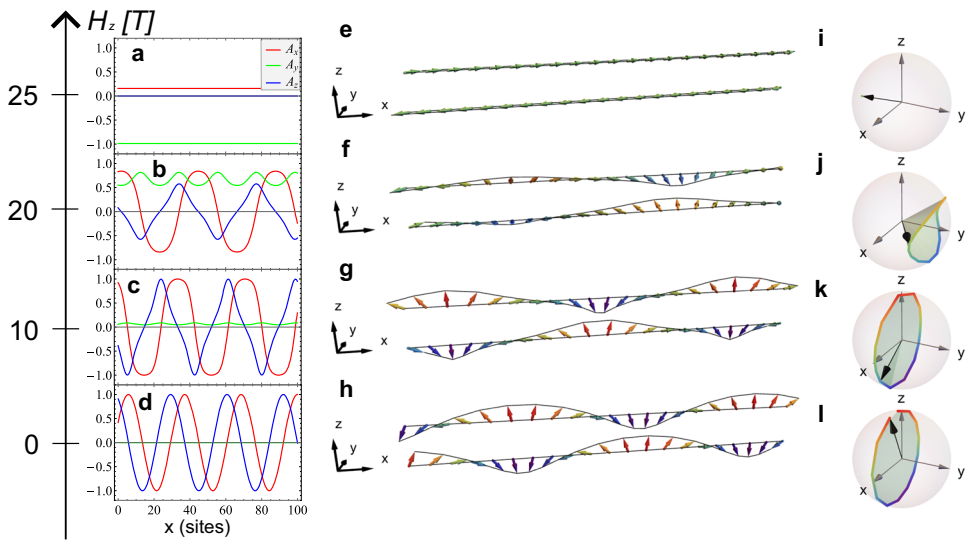


**Fig. 4 | Spin-spiral evolution by an external magnetic field as obtained from our continuous spin model. a–d** Continuous spin, **e–h** real space continuous spin textures and (**i–l**) sphere area covered by each spin array as calculated using the continuous model Eq. (37) at several external magnetic field strengths $H_z$. **a**, **e**, **i** SF state; (**b**, **f**, **j**): conical spiral; (**c**, **g**, **k**): kink state; (**d**, **h**, **l**): flat spiral state.

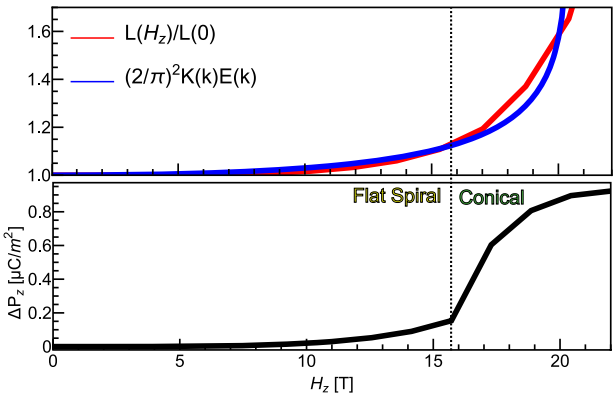


**Fig. 5 | The response to an external magnetic field $H_z$, applied along the three-fold axis in NISO.** (Upper panel) Spin spiral period calculated from the continuous model (red line) and using the analytical formula in ref. 35 (blue line). (Lower panel) magnetically-induced polarization resulting from the isotropic exchange striction. The dotted line indicates phase transition between the flat spiral state and the conical state shown in Fig. 6.

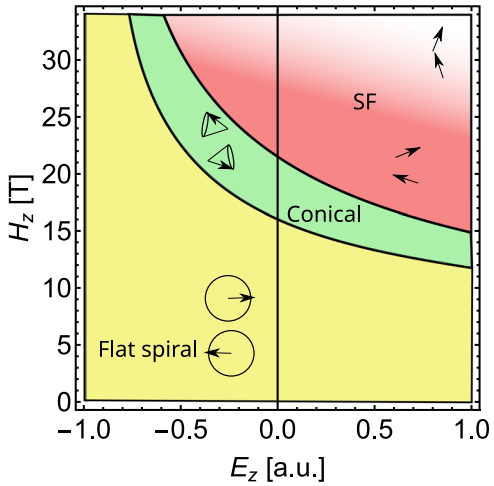


**Fig. 6 | Phase diagram of NISO as obtained by minimization of the continuous model, Eq. (37), with a small electric field $E_z$.** Yellow, green, and red areas are indicating flat spiral phase, conical phase, and SF phase, respectively. The tendency towards FM state is indicated with white in color gradients.

In the kink array phase, fast change of the angle $\theta$ near the kink at position $X$ results in a delta function-like change of the gradient $\frac{\partial\theta}{\partial x} \propto \delta(x - X)$. In this case, the interactions between kinks are found by solving Euler-Lagrange equation for the magnetic structure deformation, induced by the soliton, and result in the following interaction between kinks,

$$V(r) = \left(\frac{D}{4\beta J}\right) e^{-\beta r}, \tag{11}$$

where $\beta = \sqrt{H_z/J}$, and $r$ is the distance between the kinks. This Yukawa-like interaction can be understood as a long-range repulsion caused by exchanging virtual massive magnons (similar to how Coulomb interaction is caused by exchanges of virtual massless photons). High magnetic field results in the enlargement of the area with $\vec{A} \perp \vec{H}$ because of the exponential dependence on $H_z$ in Eq. (11). This is reminiscent of physics found in multiferroic $TbFeO_3$[36].

Figure 5 illustrates the relationship between spiral period and the polarization change. Our continuous theory predicts a period change that closely matches De Gennes's analytical formula Eq. (10). Then, the difference in the polarization (computed as a dipole moment of the cluster in Fig. 1c divided by the volume) between spiral and SF states is given as:

$$\Delta P_z^{\mathrm{iso}} = P_{\mathrm{SF},z}^{\mathrm{iso}} - P_{\mathrm{spiral},z}^{\mathrm{iso}} \approx \pi^2 \delta q^2 (p_1^{\perp} + p_2^{\perp}). \tag{12}$$

The model parameters result in a very small change due to the isotropic exchange, $\Delta P_z^{\mathrm{iso}} = 0.923\ \mu C/m^2$. Such a minor polarization change is likely to be imperceptible in experiments. In the first step (flat spiral phase), a change in polarization is induced by a change in the spiral period (kink distance). In the second step (conical phase, above 16 T, indicated by a dotted line in Fig. 5), the curve shows a sharp increase of polarization resulting from a ferromagnetic component developing in $xy$-plane due to the SF contribution.

Figure 6 illustrates the phase diagram in the ($H_z$, $E_z$) plane. Here we account for the electric field perturbatively by introducing the lowest order energy density correction $-E_z P_z$. We find that a small electric field along the ferroelectric polarization stabilizes SF state while an opposite field favors the flat spiral. Asymmetry with respect to the sign of $E_z$ is caused by the non-centrosymmetric structure of NISO, with the pyroelectric polarization set by a specific cation ordering. The $P_z$ contributions from the spiral and FM states are opposite, therefore they are stabilized by opposite electric fields. We note that the large magnetic field continuously deforms the SF state into the FM state.

### Polarization change during spin flop-to-FM transition

Our MCS results indicate the transition from SF phase to the FM state as we apply an external magnetic field (Fig. 7a). Notably, the experimental data reveals a much greater polarization change during this transition when compared to the change between the spiral and the SF phases. During this process, we can express the isotropic exchange contribution to the polarization as follows:

$$P_z^{\mathrm{iso}} = 3\cos(2\theta)(p_1^{\perp} + p_2^{\perp}), \tag{13}$$

where $\theta$ is the angle between the spin and the $xy$-plane. In our MCS this angle exhibits a linear dependence on the external magnetic field strength, as depicted in Fig. 7b. This linear dependence is also found in the experiment[16]. Consequently, we anticipate that the magnetically-induced polarization will resemble the behavior shown in Fig. 7c.

Importantly, the magnitude of this polarization change far exceeds that observed during the spiral → SF phase transition. The polarization change across the sequence of phase transitions, spiral → conical spiral → SF → FM, reproduces well the experimental data[16].

## Discussion

Our study of the complex interplay of magnetic and electric fields, magnetic exchanges and DM interactions in corundum nickelate derivative NISO has uncovered intriguing properties of multiferroic kinks and their implications for the field of MFs. The methodological advancements allowed a quantitative modelling of key magnetoelectric phenomena in NISO.

We have derived analytical formulas for magnetic exchanges and magnetically-induced polarization, starting from a minimal 2-orbital model, suitable for computing these parameters from first principles. These formulas can be applied to other $S = 1$ MFs (e.g. $Ni_3TeO_6$, $Ni_2ScSbO_6$). Additionally, we have developed a continuous theory to address complex changes in the spin-spiral structures, which extends our understanding of spiral MFs. This theory should be applicable to a wide class of materials where spiral state is stabilized by Dzyaloshinskii-Moriya interactions, for example $BiFeO_3$. Our analysis starts from the ground state with spiral ordering within the layers. We find that a spiral structure deforms into an array of multiferroic kinks upon the application of an external magnetic field in the plane of the spiral. These kinks play a crucial role in determining the period of the spiral, leading to a small polarization that is opposite to the FM

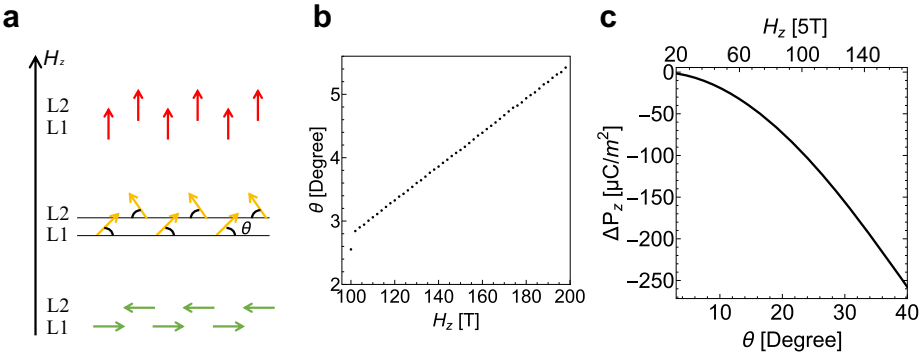


**Fig. 7 | Schematics for the SF transition and the resulting magnetically-induced polarization.** **a** Schematic representation of the SF phase. The arrows indicate spins in each layer. **b** Evolution of the angle $\theta$ after SF transition under the external magnetic field as obtained from the MCS. **c** Polarization change during the transition from SF phase to FM state.

contribution. Importantly, external magnetic fields can directly control the distances between these kinks. When a greater magnetic field is applied parallel to the three-fold axis, it induces the SF transition, consistent with experimental observations.

Using analytical and numerical models with parameters calculated from first principles, we have identified a three-step phase transition (spiral → conical spiral → SF → FM) under an applied magnetic field. Our ab-initio model shows that the most important mechanism of the magnetically-induced polarization in NISO is the isotropic exchange striction. During the first phase transition, the polarization undergoes a small change, closely related to the magnetic kink distance (spiral period). The kink density produces a contribution to the polarization that opposes the ferromagnetic contribution, resulting in polarization change similar to the spiral period change. In the second step, the polarization curve shows a sharp increase related to the FM component development in the *xy*-plane due to SF contribution. In the third step, the polarization changes significantly, simultaneously with the linear change of the canting angle $\theta$ with the magnetic field. These polarization changes imply the possibility of switching between these magnetic structures by an external electric field, enabling the electric control of magnetism. The proposed scenario is supported by the excellent agreement with the experimental data on the field dependence of the polarization.

In summary, the work advances the understanding of magnetoelectric effect in spiral multiferroics. NISO shows a rich phase diagram with flat spiral ground state, magnetic kink arrays, conical kink phase and SF phase. We reveal their connection to the magnetically-induced polarization, and the possibility of electric switching between magnetic phases via an external electric field. Given the importance of the manipulation of the spiral MFs by external fields, we expect that our findings will motivate new experiments and facilitate the applications of spiral MFs in the next-generation memory and spintronic devices.

## Methods

### First principles calculations

Density functional theory calculations have been performed for the experimental crystal structure[10] (see Fig. 1a for the hexagonal cell) using a rhombohedral cell. These calculations employed norm-conserving pseudopotentials within the Quantum ESPRESSO package[37]. The plane wave cutoff was set to 1088 eV, the Brillouin zone was sampled by a $7\times7\times7$ Monkhorst-Pack k-point mesh.

The hopping parameters of Eq. (1) is calculated using the Maximally Localized Wannier Fucntion (MLWF) technique[38] as implemented in the Wannier90 code[39–41].

The screened Coulomb and exchange interactions of Eq. (1) are calculated using constrained RPA technique[42], which yields $U = 2.3$ eV and $J_H = 0.6$ eV.

The crystal structures were visualised with VESTA[43].

### Analytical formula for the parameters of spin models

The second order perturbation energy with respect to electron hopping in the 2-orbital model is formulated as:

$$E^{(2)} = -\frac{1}{\Delta E}\sum_{\alpha,\beta}^{1,2}\left(|\langle\alpha-,i|\hat{t}_{ij}|\beta+,j\rangle|^2 + |\langle\alpha-,j|\hat{t}_{ji}|\beta+,i\rangle|^2\right), \tag{14}$$

where $|\alpha+(-),i\rangle$ indicates occupied (unoccupied) spin-orbital at site $i$ and $\Delta E = U + J_H$. Now, we assume Hamiltonian matrix elements $\hat{t}_{ij}$ are ordered as $|1\rangle|2\rangle$ (pairs of Kramers' states). Consequently, the corresponding orbital ket vectors are straightforwardly defined as: $|1\rangle = \binom{1}{0}$ and $|2\rangle = \binom{0}{1}$. Furthermore, when considering the occupied and unoccupied spin states, we assume them to have general spinor functions:

$$|-\rangle = \begin{pmatrix} -\sin\frac{\theta}{2}e^{-i\phi} \\ \cos\frac{\theta}{2} \end{pmatrix} \tag{15}$$

and

$$|+\rangle = \begin{pmatrix} \cos\frac{\theta}{2} \\ \sin\frac{\theta}{2}e^{i\phi} \end{pmatrix}. \tag{16}$$

These states have the maximal spin projection in the direction of an associated classical spin $\vec{e} = \langle+|\hat{\vec{\sigma}}|+\rangle = (\sin\theta\cos\phi, \sin\theta\sin\phi, \cos\theta)$.

Next, we decompose general $4\times4$ hopping matrices (with the proper phase) into their orbital and spin components, as described by the following equations:

$$\hat{t}_{ij} = \hat{T}^0_{ij}\otimes\hat{\sigma}_0 + \sum_{\gamma}^{x,y,z} i\hat{T}^{\gamma}_{ij}\otimes\hat{\sigma}_{\gamma}, \tag{17}$$

with the orbital part

$$\hat{T}^{\eta}_{ij} = \begin{pmatrix} t^{\eta 11}_{ij} & t^{\eta 12}_{ij} \\ t^{\eta 21}_{ij} & t^{\eta 22}_{ij} \end{pmatrix}, (\eta = 0, x, y, z) \tag{18}$$

where $\hat{\sigma}_0$ is the $2\times2$ identity matrix and $\hat{\sigma}_{\gamma}; \gamma = x, y, z$ are the spin Pauli matrices. Here, we choose the phases such that non-SOC related terms are represented solely by pure real coefficients, while SOC terms are represented solely by pure imaginary coefficients. Then, taking energy difference for different spin orientations and mapping, it is straightforward to find analytical formual Eq. (6).

The spin model can also be derived with respect to spin operators acting on $S = 1$ multiplets. The procedure is simply finding the correspondence between a general spin Hamiltonian:

$$\mathcal{H}_s = \hat{\mathbf{S}}_i \cdot \vec{\mathbb{J}}_{ij} \cdot \hat{\mathbf{S}}_j, \tag{19}$$

and the second order perturbation energy:

$$\mathcal{H}_{\text{eff}} = -\sum_{jM} \frac{1}{\Delta E_{jM}} \hat{\mathcal{T}}_{ij} |jM\rangle\langle jM| \hat{\mathcal{T}}_{ji}. \tag{20}$$

Here, $\vec{\mathbb{J}}_{ij}$ is a $3\times3$ tensor, $\hat{\mathcal{T}} ij$ is a hopping integral defined as: $\hat{\mathcal{T}}_{ij} = \sum_{\alpha\beta}\sum_{\sigma\sigma'} t_{ij}^{\alpha\beta\sigma\sigma'} \hat{c}_{i\alpha\sigma}^{\dagger} \hat{c}_{j\beta\sigma'}$ and $|jM\rangle$ represents the intermediate states $|1/2, m_1\rangle \otimes |1/2, m_2\rangle \otimes |1/2, m_3\rangle \in S = 1/2$ at site $j$. For instance, $\langle 0,1|\mathcal{H}_{\text{eff}}|1,1\rangle = \frac{1}{\sqrt{2}}(J_{ij}^{xz} + iJ_{ij}^{yz})$. This approach results in the following expressions:

$$J_{ij}^{xx} = +\frac{1}{2}\frac{1}{\Delta E}\sum_{\alpha,\beta}^{1,2}\left(+t_{ij}^{\alpha\beta\uparrow\downarrow}\left(t_{ij}^{\alpha\beta\downarrow\uparrow}\right)^* + t_{ij}^{\alpha\beta\uparrow\uparrow}\left(t_{ij}^{\alpha\beta\downarrow\downarrow}\right)^* + t_{ij}^{\alpha\beta\downarrow\downarrow}\left(t_{ij}^{\alpha\beta\uparrow\uparrow}\right)^* + t_{ij}^{\alpha\beta\downarrow\uparrow}\left(t_{ij}^{\alpha\beta\uparrow\downarrow}\right)^*\right) \tag{21}$$

$$J_{ij}^{xy} = -\frac{i}{2}\frac{1}{\Delta E}\sum_{\alpha,\beta}^{1,2}\left(-t_{ij}^{\alpha\beta\uparrow\downarrow}\left(t_{ij}^{\alpha\beta\downarrow\uparrow}\right)^* + t_{ij}^{\alpha\beta\uparrow\uparrow}\left(t_{ij}^{\alpha\beta\downarrow\downarrow}\right)^* - t_{ij}^{\alpha\beta\downarrow\downarrow}\left(t_{ij}^{\alpha\beta\uparrow\uparrow}\right)^* + t_{ij}^{\alpha\beta\downarrow\uparrow}\left(t_{ij}^{\alpha\beta\uparrow\downarrow}\right)^*\right) \tag{22}$$

$$J_{ij}^{xz} = -\frac{1}{2}\frac{1}{\Delta E}\sum_{\alpha,\beta}^{1,2}\left(+t_{ij}^{\alpha\beta\downarrow\downarrow}\left(t_{ij}^{\alpha\beta\uparrow\downarrow}\right)^* - t_{ij}^{\alpha\beta\downarrow\uparrow}\left(t_{ij}^{\alpha\beta\uparrow\uparrow}\right)^* + t_{ij}^{\alpha\beta\uparrow\downarrow}\left(t_{ij}^{\alpha\beta\downarrow\downarrow}\right)^* - t_{ij}^{\alpha\beta\uparrow\uparrow}\left(t_{ij}^{\alpha\beta\downarrow\uparrow}\right)^*\right) \tag{23}$$

$$J_{ij}^{yx} = -\frac{i}{2}\frac{1}{\Delta E}\sum_{\alpha,\beta}^{1,2}\left(-t_{ij}^{\alpha\beta\uparrow\downarrow}\left(t_{ij}^{\alpha\beta\downarrow\uparrow}\right)^* - t_{ij}^{\alpha\beta\uparrow\uparrow}\left(t_{ij}^{\alpha\beta\downarrow\downarrow}\right)^* + t_{ij}^{\alpha\beta\downarrow\downarrow}\left(t_{ij}^{\alpha\beta\uparrow\uparrow}\right)^* + t_{ij}^{\alpha\beta\downarrow\uparrow}\left(t_{ij}^{\alpha\beta\uparrow\downarrow}\right)^*\right) \tag{24}$$

$$J_{ij}^{yy} = +\frac{1}{2}\frac{1}{\Delta E}\sum_{\alpha,\beta}^{1,2}\left(-t_{ij}^{\alpha\beta\uparrow\downarrow}\left(t_{ij}^{\alpha\beta\downarrow\uparrow}\right)^* + t_{ij}^{\alpha\beta\uparrow\uparrow}\left(t_{ij}^{\alpha\beta\downarrow\downarrow}\right)^* + t_{ij}^{\alpha\beta\downarrow\downarrow}\left(t_{ij}^{\alpha\beta\uparrow\uparrow}\right)^* - t_{ij}^{\alpha\beta\downarrow\uparrow}\left(t_{ij}^{\alpha\beta\uparrow\downarrow}\right)^*\right) \tag{25}$$

$$J_{ij}^{yz} = +\frac{i}{2}\frac{1}{\Delta E}\sum_{\alpha,\beta}^{1,2}\left(+t_{ij}^{\alpha\beta\downarrow\downarrow}\left(t_{ij}^{\alpha\beta\uparrow\downarrow}\right)^* - t_{ij}^{\alpha\beta\downarrow\uparrow}\left(t_{ij}^{\alpha\beta\uparrow\uparrow}\right)^* - t_{ij}^{\alpha\beta\uparrow\downarrow}\left(t_{ij}^{\alpha\beta\downarrow\downarrow}\right)^* + t_{ij}^{\alpha\beta\uparrow\uparrow}\left(t_{ij}^{\alpha\beta\downarrow\uparrow}\right)^*\right) \tag{26}$$

$$J_{ij}^{zx} = -\frac{1}{2}\frac{1}{\Delta E}\sum_{\alpha,\beta}^{1,2}\left(-t_{ij}^{\alpha\beta\uparrow\uparrow}\left(t_{ij}^{\alpha\beta\uparrow\downarrow}\right)^* + t_{ij}^{\alpha\beta\downarrow\uparrow}\left(t_{ij}^{\alpha\beta\downarrow\downarrow}\right)^* - t_{ij}^{\alpha\beta\uparrow\downarrow}\left(t_{ij}^{\alpha\beta\uparrow\uparrow}\right)^* + t_{ij}^{\alpha\beta\downarrow\downarrow}\left(t_{ij}^{\alpha\beta\downarrow\uparrow}\right)^*\right) \tag{27}$$

$$J_{ij}^{zy} = +\frac{i}{2}\frac{1}{\Delta E}\sum_{\alpha,\beta}^{1,2}\left(-t_{ij}^{\alpha\beta\uparrow\uparrow}\left(t_{ij}^{\alpha\beta\uparrow\downarrow}\right)^* + t_{ij}^{\alpha\beta\downarrow\uparrow}\left(t_{ij}^{\alpha\beta\downarrow\downarrow}\right)^* + t_{ij}^{\alpha\beta\uparrow\downarrow}\left(t_{ij}^{\alpha\beta\uparrow\uparrow}\right)^* - t_{ij}^{\alpha\beta\downarrow\downarrow}\left(t_{ij}^{\alpha\beta\downarrow\uparrow}\right)^*\right) \tag{28}$$

$$J_{ij}^{zz} = +\frac{1}{2}\frac{1}{\Delta E}\sum_{\alpha,\beta}^{1,2}\left(-|t_{ij}^{\alpha\beta\uparrow\downarrow}|^2 - |t_{ij}^{\alpha\beta\downarrow\uparrow}|^2 + |t_{ij}^{\alpha\beta\uparrow\uparrow}|^2 + |t_{ij}^{\alpha\beta\downarrow\downarrow}|^2\right), \tag{29}$$

where the difference in signs between the second-order energies arises from particle exchanges. This tensor can generally be decomposed into isotropic interaction: $J_{ij} = -\frac{1}{3}\text{Tr}\vec{\mathbb{J}}_{ij}$, Dzhaloshinskii-Moriya vectors: $\vec{D}_{ij} = \frac{1}{2}\begin{pmatrix} J_{ij}^{yz} - J_{ij}^{zy} \\ J_{ij}^{zx} - J_{ij}^{xz} \\ J_{ij}^{xy} - J_{ij}^{yx} \end{pmatrix}$, and symmetric anisotropy: $\vec{\Gamma}_{ij} = \frac{1}{2}\left(\vec{\mathbb{J}}_{ij} + \vec{\mathbb{J}}^{\text{t}}_{ij}\right) - J_{ij}\vec{\mathbb{I}}$. However, this approach results in the exactly same result as the classical vector approach Eq. (6). The equivalence of the two approaches can be easily demonstrated by considering the relationship between the hopping integrals For example,

$$t_{ij}^{\alpha\beta\uparrow\uparrow} = t_{ij}^{0\alpha\beta} + it_{ij}^{z\alpha\beta}.$$

Substituting this definition into Eq. (9–17) yields the same formula as Eq. (6). Here, we provide an explicit notation for the diagonal elements as an example:

$$\begin{aligned} J_{ij}^{xx} &= +\tfrac{1}{2}\tfrac{1}{\Delta E}\sum_{\alpha,\beta}^{1,2}\left(+t_{ij}^{\alpha\beta\uparrow\downarrow}\left(t_{ij}^{\alpha\beta\downarrow\uparrow}\right)^* + t_{ij}^{\alpha\beta\uparrow\uparrow}\left(t_{ij}^{\alpha\beta\downarrow\downarrow}\right)^* + t_{ij}^{\alpha\beta\downarrow\downarrow}\left(t_{ij}^{\alpha\beta\uparrow\uparrow}\right)^* + t_{ij}^{\alpha\beta\downarrow\uparrow}\left(t_{ij}^{\alpha\beta\uparrow\downarrow}\right)^*\right) \\ &= \tfrac{1}{\Delta E}\sum_{\alpha,\beta}^{1,2}\left(\left(t_{ij}^{0\alpha\beta}\right)^2 + \left(t_{ij}^{x\alpha\beta}\right)^2 - \left(t_{ij}^{y\alpha\beta}\right)^2 - \left(t_{ij}^{z\alpha\beta}\right)^2\right), \\ J_{ij}^{yy} &= +\tfrac{1}{2}\tfrac{1}{\Delta E}\sum_{\alpha,\beta}^{1,2}\left(-t_{ij}^{\alpha\beta\uparrow\downarrow}\left(t_{ij}^{\alpha\beta\downarrow\uparrow}\right)^* + t_{ij}^{\alpha\beta\uparrow\uparrow}\left(t_{ij}^{\alpha\beta\downarrow\downarrow}\right)^* + t_{ij}^{\alpha\beta\downarrow\downarrow}\left(t_{ij}^{\alpha\beta\uparrow\uparrow}\right)^* - t_{ij}^{\alpha\beta\downarrow\uparrow}\left(t_{ij}^{\alpha\beta\uparrow\downarrow}\right)^*\right) \\ &= \tfrac{1}{\Delta E}\sum_{\alpha,\beta}^{1,2}\left(\left(t_{ij}^{0\alpha\beta}\right)^2 + \left(t_{ij}^{y\alpha\beta}\right)^2 - \left(t_{ij}^{x\alpha\beta}\right)^2 - \left(t_{ij}^{z\alpha\beta}\right)^2\right), \\ J_{ij}^{zz} &= +\tfrac{1}{2}\tfrac{1}{\Delta E}\sum_{\alpha,\beta}^{1,2}\left(-\left|t_{ij}^{\alpha\beta\uparrow\downarrow}\right|^2 - \left|t_{ij}^{\alpha\beta\downarrow\uparrow}\right|^2 + \left|t_{ij}^{\alpha\beta\uparrow\uparrow}\right|^2 + \left|t_{ij}^{\alpha\beta\downarrow\downarrow}\right|^2\right) \\ &= \tfrac{1}{\Delta E}\sum_{\alpha,\beta}^{1,2}\left(\left(t_{ij}^{0\alpha\beta}\right)^2 + \left(t_{ij}^{z\alpha\beta}\right)^2 - \left(t_{ij}^{x\alpha\beta}\right)^2 - \left(t_{ij}^{y\alpha\beta}\right)^2\right). \end{aligned}$$

Therefore, the isotropic interaction is given as

$$J_{ij} = -\tfrac{1}{3}\text{Tr}\vec{\mathbb{J}}_{ij} = \tfrac{1}{3\Delta E}\sum_{\alpha\beta}^{1,2}\left\{-3\left(t_{ij}^{0\alpha\beta}\right)^2 + \text{Tr}(\mathbf{t}_{ij}^{\alpha\beta} \otimes \mathbf{t}_{ij}^{\alpha\beta})\right\}.$$

All the other expression can be restored following the same procedure.

A similar theory can be developed for magnetically induced electronic polarization. The main idea is to expand the Wannier functions with respect to first-order of the hopping and apply the general theory of electronic polarization in solids. This expansion corresponds to spin-dependent modulations of the Wannier density, resulting in changes in the Wannier centers. Starting point of the theory is the general theory for polarization in solids[23]:

$$\vec{P} = -\frac{e}{V}\sum_{i}^{\text{occ}}\langle w_i|\hat{r}|w_i\rangle, \tag{30}$$

where $\langle w_i|\hat{r}|w_i\rangle$ represents the position operator's diagonal elements in the Wannier basis, and $V$ is the cell volume. Next, the first-order perturbation expansion of the Wannier function with respect to electron hopping is:

$$|w_i\rangle \approx |\alpha+, i\rangle - \frac{1}{\Delta E}\sum_{j}\sum_{\beta}^{1,2}|\beta-, j\rangle\langle\beta-, j|\hat{t}_{ji}|\alpha+, i\rangle. \tag{31}$$

By substituting Eq. (31) into Eq. (30), we obtain pair and single-ion terms as $\vec{P} = \sum_i \vec{P}_i + \sum_{<ij>}\vec{P}_{ij}$. The pair interaction terms are as follows:

$$\begin{aligned} \vec{P}_{ij} = \tfrac{e}{V\Delta E}\sum_{\alpha\beta}^{1,2} \Big[&\langle\alpha+, i|\hat{\vec{r}}_{ij}|\beta-, j\rangle\langle\beta-, j|\hat{t}_{ji}|\alpha+, i\rangle + \langle\alpha+, i|\hat{t}_{ij}|\beta-, j\rangle\langle\beta-, j|\hat{\vec{r}}_{ji}|\alpha+, i\rangle \\ &+\langle\alpha+, j|\hat{\vec{r}}_{ji}|\beta-, i\rangle\langle\beta-, i|\hat{t}_{ji}|\alpha+, j\rangle + \langle\alpha+, j|\hat{t}_{ji}|\beta-, i\rangle\langle\beta-, i|\hat{\vec{r}}_{ij}|\alpha+, j\rangle\Big]. \end{aligned} \tag{32}$$

Similar to the hopping matrix, the position matrix can be decomposed into a linear combination of the Pauli matrices as:

$$\hat{\vec{r}}_{ij} = \hat{\vec{R}}^{0}_{ij} \otimes \sigma_0 + \sum_{\gamma'} i\hat{\vec{R}}^{\gamma'}_{ij} \otimes \hat{\sigma}_{\gamma'}. \tag{33}$$

Then, it is straightforward to find the pair interaction formula Eq. (3) and the corresponding analytical formula Eq. (7).

### Single-*q* spiral ansatz

In the simplest approximation, a spin-spiral state can be characterized by a single $q$-vector,

$$\vec{e}_i = \hat{n}_1 \cos(\vec{q}\cdot\vec{R}_i) + \hat{n}_2 \sin(\vec{q}\cdot\vec{R}_i), \tag{34}$$

where $\hat{n}_1$ and $\hat{n}_2$ are orthogonal vectors within the plane of the spiral, $\vec{q}$ is the propagation vector and $\vec{R}_i$ is the vector pointing to the site $i$. This is an Ansatz of a single-$q$ spiral state. The spiral plane can be characterized by its normal vector,

$$\hat{n}^{\perp} = (-\sin\phi, \cos\phi, 0), \tag{35}$$

where $\phi$ indicates the rotation of the spin-spiral plane. In this case, the relative orientation between $\delta\vec{q}$ and $\hat{n}^{\perp}$ defines the spiral type. For instance, $\delta\vec{q} \parallel \hat{n}^{\perp}$ is a proper-screw spiral state.

### Layer AFM chain continuous model

We express magnetization and AFM order parameter at position $x$ as $\vec{M}(x) = \vec{S}_1(x) + \vec{S}_2(x)$ and $\vec{A}(x) = \vec{S}_1(x) - \vec{S}_2(x)$, respectively. In this formulas, $\vec{S}_1(x)$ and $\vec{S}_2(x)$ are spins at neighboring layer $L1$ and $L2$ and these satisfy $\vec{A}(x)\cdot\vec{M}(x) = 0$. Then, energy density of the chain at position $x$ is expressed as

$$\delta E(x) = -\tfrac{J'}{4}\left(\nabla\vec{A}(x)\right)^2 + \vec{D}\cdot\left[\vec{A}(x)\times\left(\nabla\vec{A}(x)\right)\right] - \vec{H}\cdot\vec{M}(x) + J. \tag{36}$$

In this equation, the first term is the effective isotropic ferromagnetic exchange, $J' < 0$, the second one is the antisymmetric DM interaction, the third term corresponds to the Zeeman energy due to an external field $\vec{H}$, and the last term is the energy of a ferromagnetic state. The alternating inter-layer AFM exchange coupling in NISO can be considered as intra-layer FM exchanges. Considering inter-layer AFM exchange $J$, the effective intra-layer FM exchange would be $J' = -2J$. By employing the Fourier expansion of the spin, $\vec{A}(x) = \frac{1}{\sqrt{N}}\sum_{n=-N}^{N}\vec{A}_n\, e^{iQnx}$, we obtain a simplified energy expression that has to be minimized:

$$\begin{aligned} E_{\mathrm{rec}} = &\sum_{n=-N}^{N}\left[-\tfrac{J'}{4}Q^2n^2\vec{A}_n\cdot\vec{A}_{-n} + i\vec{D}Qn\cdot\left(\vec{A}_{-n}\times\vec{A}_n\right)\right] - \left(\vec{H}\cdot\vec{A}_0\right)^2 \\ &+\lambda\left(\sum_{l'm'n'p'} e^{iQ(l'+m'+n'+p')x}\vec{A}_{l'}\vec{A}_{m'}\vec{A}_{n'}\vec{A}_{p'} - 2\vec{A}_n\vec{A}_{-n}\right), \end{aligned} \tag{37}$$

where the last term is the energy penalty with coefficient $\lambda \gg 1$ enforcing a constraint on the spin length. Similarly, the change of the spin-isotropic part of the polarization per spin can be evaluated as:

$$P_z^{\mathrm{iso}} \propto -1 + \sum_{n=-N}^{N} Q^2n^2\vec{A}_n\cdot\vec{A}_{-n}. \tag{38}$$

## Data availability

The datasets used and/or analyzed during the current study are available from the corresponding author upon reasonable request.

Received: 17 November 2023; Accepted: 7 March 2024;
Published online: 03 June 2024

## References

1. Kimura, T. et al. Magnetic control of ferroelectric polarization. *Nature* **426**, 55–58 (2003).
2. Tokura, Y. & Seki, S. Multiferroics with spiral spin orders. *Adv. Mater.* **22**, 1554–1565 (2010).
3. Tokura, Y., Seki, S. & Nagaosa, N. Multiferroics of spin origin. *Rep. Progr. Phys.* **77**, 076501 (2014).
4. Khomskii, D. Classifying multiferroics: mechanisms and effects. *Physics* **2**, 20 (2009).
5. Cheong, S.-W. & Mostovoy, M. Multiferroics: a magnetic twist for ferroelectricity. *Nat. Mater.* **6**, 13–20 (2007).
6. Fiebig, M., Lottermoser, T., Meier, D. & Trassin, M. The evolution of multiferroics. *Nat. Rev. Mater.* **1**, 16046 (2016).
7. Seki, S., Ishiwata, S. & Tokura, Y. Magnetoelectric nature of skyrmions in a chiral magnetic insulator $Cu_2OSeO_3$. *Phys. Rev. B* **86**, 060403 (2012).
8. Ruff, E. et al. Multiferroicity and skyrmions carrying electric polarization in $GaV_4S_8$. *Sci. Adv.* **1**, e1500916 (2015).
9. Ivanov, S. A. et al. Spin and dipole ordering in $Ni_2InSbO_6$ and $Ni_2ScSbO_6$ with corundum-related structure. *Chem. Mater.* **25**, 935–945 (2013).
10. Weil, M., Mathieu, R., Nordblad, P. & Ivanov, S. Crystal growth experiments in the systems $Ni_2MSbO_6$ (M = Sc, In) using chemical vapour transport reactions: $Ni_2InSbO_6$ and $NiSb_2O_6$ crystals in the millimetre range. *Crystal Res. Technol.* **49**, 142–151 (2014).
11. Kim, J. W. et al. Successive magnetic-field-induced transitions and colossal magnetoelectric effect in $Ni_3TeO_6$. *Phys. Rev. Lett.* **115**, 137201 (2015).
12. Yokosuk, M. O. et al. Magnetoelectric coupling through the spin flop transition in $Ni_3TeO_6$. *Phys. Rev. Lett.* **117**, 147402 (2016).
13. Cai, G.-H., Greenblatt, M. & Li, M.-R. Polar magnets in double corundum oxides. *Chem. Mater.* **29**, 5447–5457 (2017).
14. Frank, C. E. et al. $Fe_{3-x}InSn_xO_6$ (x = 0, 0.25, or 0.5): a family of corundum derivatives with sn-induced polarization and above room temperature antiferromagnetic ordering. *Chem. Mater.* **34**, 5020–5029 (2022).
15. Ye, M. & Vanderbilt, D. Ferroelectricity in corundum derivatives. *Phys. Rev. B* **93**, 134303 (2016).
16. Araki, Y. et al. Metamagnetic transitions and magnetoelectric responses in the chiral polar helimagnet $Ni_2InSbO_6$. *Phys. Rev. B* **102**, 054409 (2020).
17. Liu, Z. et al. Spin excitation in the coupled honeycomb lattice compound $Ni_2InSbO_6$. *Phys. Rev. B* **107**, 064428 (2023).
18. Ihara, Y. et al. Field-induced magnetic structures in the chiral polar antiferromagnet $Ni_2InSbO_6$. *Phys. Rev. B* **108**, 024417 (2023).
19. Choi, Y. J. et al. Ferroelectricity in an ising chain magnet. *Phys. Rev. Lett.* **100**, 047601 (2008).
20. Katsura, H., Nagaosa, N. & Balatsky, A. V. Spin current and magnetoelectric effect in noncollinear magnets. *Phys. Rev. Lett.* **95**, 057205 (2005).
21. Arima, T. Ferroelectricity induced by proper-screw type magnetic order. *J. Phys. Soc. Japan* **76**, 073702 (2007).
22. King-Smith, R. D. & Vanderbilt, D. Theory of polarization of crystalline solids. *Phys. Rev. B* **47**, 1651–1654 (1993).
23. Vanderbilt, D. & King-Smith, R. D. Electric polarization as a bulk quantity and its relation to surface charge. *Phys. Rev. B* **48**, 4442–4455 (1993).
24. Resta, R. Electrical polarization and orbital magnetization: the modern theories. *J. Phys. Condensed Matter* **22**, 123201 (2010).
25. Perdew, J. P., Burke, K. & Ernzerhof, M. Generalized gradient approximation made simple. *Phys. Rev. Lett.* **77**, 3865–3868 (1996).
26. Perdew, J. P., Burke, K. & Ernzerhof, M. Generalized gradient approximation made simple. *Phys. Rev. Lett.* **78**, 1396–1396 (1997).
27. Kanamori, J. Electron correlation and ferromagnetism of transition metals. *Progr. Theor. Phys.* **30**, 275–289 (1963).
28. Moriya, T. Anisotropic superexchange interaction and weak ferromagnetism. *Phys. Rev.* **120**, 91–98 (1960).

29. Nikolaev, S. A. & Solovyev, I. V. Microscopic theory of electric polarization induced by skyrmionic order in $GaV_4S_8$. *Phys. Rev. B* **99**, 100401 (2019).
30. Ono, R., Nikolaev, S. & Solovyev, I. Fingerprints of spin-current physics on magnetoelectric response in the spin-$\frac{1}{2}$ magnet $Ba_2CuGe_2O_7$. *Phys. Rev. B* **102**, 064422 (2020).
31. Solovyev, I., Ono, R. & Nikolaev, S. Magnetically induced polarization in centrosymmetric bonds. *Phys. Rev. Lett.* **127**, 187601 (2021).
32. Solovyev, I. V. Magnetization-induced local electric dipoles and multiferroic properties of $Ba_2CoGe_2O_7$. *Phys. Rev. B* **91**, 224423 (2015).
33. Goodenough, J. B. Theory of the role of covalence in the perovskite-type manganites [La, *M*(II)]$MnO_3$. *Phys. Rev.* **100**, 564–573 (1955).
34. Liechtenstein, A., Katsnelson, M., Antropov, V. & Gubanov, V. Local spin density functional approach to the theory of exchange interactions in ferromagnetic metals and alloys. *J. Magn. Magn. Mater.* **67**, 65–74 (1987).
35. De Gennes, P. Calcul de la distorsion d'une structure cholesterique par un champ magnetique. *Solid State Commun.* **6**, 163–165 (1968).
36. Artyukhin, S. et al. Solitonic lattice and yukawa forces in the rare-earth orthoferrite $TbFeO_3$. *Nat. Mater.* **11**, 694–699 (2012).
37. Giannozzi, P. et al. Quantum espresso: a modular and open-source software project for quantum simulations of materials. *J. Phys. Condens. Matter* **21**, 395502 (2009).
38. Marzari, N. & Vanderbilt, D. Maximally localized generalized wannier functions for composite energy bands. *Phys. Rev. B* **56**, 12847–12865 (1997).
39. Pizzi, G. et al. Wannier90 as a community code: new features and applications. *J. Phys. Condens. Matter* **32**, 165902 (2020).
40. Mostofi, A. A. et al. An updated version of wannier90: a tool for obtaining maximally-localised wannier functions. *Comput. Phys. Commun.* **185**, 2309–2310 (2014).
41. Marzari, N., Mostofi, A. A., Yates, J. R., Souza, I. & Vanderbilt, D. Maximally localized wannier functions: theory and applications. *Rev. Mod. Phys.* **84**, 1419–1475 (2012).
42. Aryasetiawan, F. et al. Frequency-dependent local interactions and low-energy effective models from electronic structure calculations. *Phys. Rev. B* **70**, 195104 (2004).
43. Momma, K. & Izumi, F. *V*ESTA: a three-dimensional visualization system for electronic and structural analysis. *J. Appl. Crystallogr.* **41**, 653–658 (2008).


## Acknowledgements

We thank M. Mostovoy and S. A. Nikolaev for fruitful discussions. R.O., was supported by JSPS KAKENHI Grant Numbers JP23KJ2165. MANA is supported by World Premier International Research Center Initiative (WPI), MEXT, Japan. The computations in this study were performed on the Numerical Materials Simulator at the NIMS and the Supercomputer Center, the Institute for Solid State Physics, the University of Tokyo.

## Author contributions

R.O. performed first-principles calculations, analytical formula derivations, MCS simulations, and 1D continuous model simulations. R.O. and I.S. performed derivation of the multiplet energy in the superexchange theory. R.O. and S.A. performed derivation of the 1D continuous model and the Yukawa-like potential. All authors participated in analyzing the data and discussions. R.O. wrote the main manuscript text with contributions from all authors.

## Competing interests

The authors declare no competing interests.

## Additional information

**Supplementary information** The online version contains supplementary material available at https://doi.org/10.1038/s44306-024-00020-9.

**Correspondence** and requests for materials should be addressed to Ryota Ono.

**Reprints and permissions information** is available at http://www.nature.com/reprints

**Publisher's note** Springer Nature remains neutral with regard to jurisdictional claims in published maps and institutional affiliations.

**Open Access** This article is licensed under a Creative Commons Attribution 4.0 International License, which permits use, sharing, adaptation, distribution and reproduction in any medium or format, as long as you give appropriate credit to the original author(s) and the source, provide a link to the Creative Commons licence, and indicate if changes were made. The images or other third party material in this article are included in the article's Creative Commons licence, unless indicated otherwise in a credit line to the material. If material is not included in the article's Creative Commons licence and your intended use is not permitted by statutory regulation or exceeds the permitted use, you will need to obtain permission directly from the copyright holder. To view a copy of this licence, visit http://creativecommons.org/licenses/by/4.0/.

© The Author(s) 2024, corrected publication 2025